

RESEARCH ARTICLE

View Article Online

View Journal | View Issue



Cite this: *Inorg. Chem. Front.*, 2023, 10, 5726

Na₆Sn₃P₄S₁₆: Sn(II)-chelated PS₄ groups inspired an ultra-strong SHG response†

Chenyao Zhao,^a Bingbing Zhang,^{*a} Xinyu Tian,^a Guoqiang Zhou,^{id} ^{*a} Jingjing Xu^a and Kui Wu^{id} ^{*b}

The discovery of new infrared nonlinear optical (IR NLO) materials with a large second harmonic generation (SHG) effect and broad optical bandgap is still a challenging task. Based on this, we propose a rational strategy for the design of new NLO materials: (i) the coupling of stereochemically active lone-pair (SCALP) Sn(II) cations and typical PS₄ units into a structure enhances the SHG response; (ii) the incorporation of an alkali metal (Na⁺) cation benefits the preservation of a relatively wide bandgap, which affords the discovery of a new promising IR NLO thiophosphate, Na₆Sn₃P₄S₁₆. It exhibits an ultra-strong SHG response (6.6 × AgGaS₂) and relatively wide bandgap (2.52 eV) that is better than those of known NLO SnPS₃ (1.1 × AgGaS₂ and 2.35 eV). Remarkably, Na₆Sn₃P₄S₁₆ exhibits the largest SHG response among all known IR NLO thiophosphates with bandgaps greater than 2.50 eV. Such an ultra-strong SHG response in Na₆Sn₃P₄S₁₆ originates from the collaborative polarization of edge-sharing SnS₄ and PS₄ units. This work inspires a new way to design new IR NLO thiophosphates with enhanced SHG responses by introducing Sn(II)-chelated PS₄ groups into structures.

Received 5th July 2023,
Accepted 18th August 2023

DOI: 10.1039/d3qi01257c

rsc.li/frontiers-inorganic

Introduction

Nonlinear optical (NLO) crystals have come to play critical roles in the fabrication of tunable lasers for the development of modern civil–military technology.^{1–7} In past decades, NLO crystals with excellent performance in the ultraviolet (UV) and visible regions (*e.g.*, β-BaB₂O₄ (β-BBO), LiB₃O₅ (LBO), KTiOPO₄ (KTP) and KH₂PO₄ (KDP)) have been rapidly developed and industrialized.^{8,9} Mid-infrared (IR) lasers have also shown significant applications in remote communication and IR detection.^{10–13} Unfortunately, a few conventional commercial IR NLO crystals, such as AgGaQ₂ (Q = S, Se)¹⁴ and ZnGeP₂,¹⁵ with several inherent defects such as a low laser damage threshold (LDT), harmful two-photon absorption and small birefringence, have hindered their range of application. Limited by the property requirements (wide IR transmission range, strong second harmonic generation (SHG) response, broad optical bandgap and large optical anisotropy) for an excellent IR NLO crystal, there is still a lack of outstanding

NLO crystals for IR applications.^{16–18} So far, extensive work has been undertaken to explore IR NLO materials and several effective design strategies have been proposed: for example, coupling highly distorted anionic units into a structure, such as various anionic groups with centered d⁰ or d¹⁰ transition metals or stereochemically active lone-pair (SCALP) cations, has been proven to have a positive impact on the SHG response.^{19–23} In addition, introducing alkali or alkaline-earth metals as cations into crystal structures can effectively broaden the optical bandgap of targeted crystals.²⁴ Recently, chalcogenides containing SCALP metal cations (Sn²⁺, Pb²⁺, As³⁺, Sb³⁺ and Bi³⁺) were selected as optimal systems to search for IR NLO materials with strong SHG effects. As for cations with SCALP, their outermost electrons are not shared with other ions that generate repulsive interactions for the formation of highly distorted polyhedral groups, which can induce positive symmetry-breaking for the potential development of NCS or even chiral structures. This SCALP strategy can definitely be beneficial for improving the probability of obtaining NCS structures, but cannot completely guarantee an NCS structure. However, SCALP cation-centered polyhedra usually exhibit large distortion and a uniform polarized arrangement, which indicates that they have huge potential for an enhancement of inherent NLO effects.^{25–30} Notably, introducing two or more types of NLO-active functional units into one structure is an effective way to strengthen the SHG effect.^{31–33} Moreover, strong covalent P–S bonds in the tetrahedral PS₄ also contribute to the improved NLO response, and a series of thiopho-

^aCollege of Chemistry and Materials Science, Hebei University, Baoding, China. E-mail: zhougq1982@163.com, zhangbb@hbu.edu.cn

^bState Key Laboratory of Crystal Materials and Institute of Crystal Materials, Shandong University, Jinan, China. E-mail: wukui@sdu.edu.cn

†Electronic supplementary information (ESI) available: Performance comparison, crystal data, structural summary, BS and DOS. CCDC 2278142. For ESI and crystallographic data in CIF or other electronic format see DOI: <https://doi.org/10.1039/d3qi01257c>

sphates have become more established as IR NLO candidates.^{34–39} On the basis of combining the above strategies, we have successfully synthesized a new NCS compound, $\text{Na}_6\text{Sn}_3\text{P}_4\text{S}_{16}$, in the thiophosphate system by coupling the SCALP cation $\text{Sn}(\text{II})$ and a PS_4 unit. $\text{Na}_6\text{Sn}_3\text{P}_4\text{S}_{16}$ exhibits a peculiar low-dimensional cluster structure consisting of edge-sharing SnS_4 and PS_4 tetrahedra. Remarkably, $\text{Na}_6\text{Sn}_3\text{P}_4\text{S}_{16}$ exhibits an ultra-strong SHG response ($6.6 \times \text{AgGaS}_2$) and a relatively wide bandgap (2.52 eV), showing the largest SHG effect among all reported IR NLO thiophosphates with a bandgap greater than 2.50 eV (Fig. 1a).^{34–37,40–51} Compared with known SnPS_3 ,⁵² $\text{Na}_6\text{Sn}_3\text{P}_4\text{S}_{16}$ also shows an obvious improvement in bandgap and SHG effect (Fig. 1b), illustrating the importance of the $\text{Sn}(\text{II})\text{S}_4$ unit for material performance. Theoretical calculation further confirms that the collaborative polarization of edge-sharing $\text{Sn}(\text{II})\text{S}_4$ and PS_4 units provides a huge contribution to the strong SHG response, which also offers us a new way to design new IR NLO candidates through coupling $\text{Sn}(\text{II})$ -chelated PS_4 groups into structures.

Experimental methods

Materials

All raw reagents (Na, SnS, P and S powder) were purchased from the Beijing Hawk Science & Technology Co., Ltd with a high-purity level (99.9%). Herein, the storage and weighing processes were carried out in an Ar-filled glovebox (the oxygen and water vapour contents were lower than 0.1 ppm) to prevent oxidation of the Na metal.

Synthesis

Microcrystals of $\text{Na}_6\text{Sn}_3\text{P}_4\text{S}_{16}$ were synthesized in a stoichiometric proportion by the high-temperature solid-state method. The detailed steps are as follows: (1) A mixture of Na (6 mmol), SnS (3 mmol), P (4 mmol), and S (13 mmol) was first weighed and loaded into a graphite crucible, then put into a silica tube; (2) The silica tube was pumped to a 10^{-3} Pa vacuum and sealed with a flame; (3) The silica tubes were placed in a muffle furnace; (4) A rising temperature program was set to heat the tube to 750 °C at 15°C h^{-1} and it was kept at this temperature for about 100 h, then slowly cooled down to room temperature

over 3 days. Finally, many millimeter-level yellow crystals for $\text{Na}_6\text{Sn}_3\text{P}_4\text{S}_{16}$ (the yield >90%) were obtained and found to be stable in air for several months.

Single crystal X-ray diffraction

Selected high-quality single crystals of $\text{Na}_6\text{Sn}_3\text{P}_4\text{S}_{16}$ were fixed on glass fibers with epoxy. Diffraction data were collected on a Bruker D8 VENTURE diffractometer using Mo $K\alpha$ radiation ($\lambda = 0.71073 \text{ \AA}$) at 296 K. The crystal structure was determined by the direct method and refined by full-matrix least-squares fitting on F^2 using the SHELXTL program package.⁵³ The PLATON program was used to verify the final structures, and no higher symmetries were found.⁵⁴ A multi-scan method was used for absorption correction. Anisotropic refinement and extinction corrections achieved rational anisotropic thermal parameters for all atoms.

Powder X-ray diffraction

In order to determine the purity of the samples, the powder X-ray diffraction (XRD) patterns of $\text{Na}_6\text{Sn}_3\text{P}_4\text{S}_{16}$ were collected using a Bruker D2 X-ray diffractometer with Cu $K\alpha$ radiation ($\lambda = 1.5418 \text{ \AA}$) at room temperature. The 2θ range was $10\text{--}70^\circ$ with a step size of 0.02° and a fixed counting time of 1 s per step. Using Mercury software, the calculated XRD patterns were derived from the respective single-crystal data. The experimental XRD patterns are consistent with the corresponding calculated patterns (Fig. 4a), indicating the purity of the samples and the accuracy of the structural model.

UV-vis-near-IR (NIR) diffuse-reflectance spectra

Diffuse-reflectance spectra were measured with a Shimadzu SolidSpec-3700DUV spectrophotometer in the wavelength range of 200–1100 nm at room temperature, with BaSO_4 as the standard reference. The absorption data were calculated using the Kubelka–Munk formula: $\alpha/S = (1 - R)^2/2R$, where α , S and R represent the absorption, scattering and reflection coefficients.

IR and Raman spectra

The infrared spectrum was carried out on a Shimadzu IR Affinity Fourier transform infrared spectrometer in the range of 400–4000 cm^{-1} with a resolution of 4 cm^{-1} . The crystals were mixed well with spectrally pure KBr in a ratio of approximately 1:100 as the sample for measurement. Then, the sample was dried and ground into a fine powder under an IR lamp. Powder samples were pressed into a transparent sheet. Finally, the sheet was loaded into the sample chamber, and the IR spectral data were recorded.

High-quality crystals were placed on object slides for measurement. Then, the Raman spectrum was recorded with a 532 nm laser using a LabRAM HR Evolution spectrometer equipped with a CCD detector. The integration time was set to 5 seconds.

Second-harmonic generation measurement

The powder SHG response was measured using the Kurtz and Perry method with a Q-switch laser (2.09 μm , 3 Hz, 50 ns). The

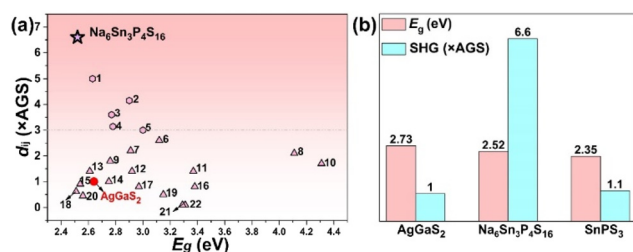


Fig. 1 (a) Summary of the SHG response and bandgap among $\text{Na}_6\text{Sn}_3\text{P}_4\text{S}_{16}$ and reported IR NLO thiophosphates with bandgaps greater than 2.50 eV. Detailed data are listed in Table S1.† (b) Histogram comparison for the NLO data of AgGaS_2 , $\text{Na}_6\text{Sn}_3\text{P}_4\text{S}_{16}$ and SnPS_3 .

polycrystalline sample was ground and sieved into different particle sizes: 38–55, 55–88, 88–105, 105–150, 150–200, and 200–250 μm . AgGaS_2 crystals with the same size range were used as the reference.

Theoretical calculations

The electronic structure and partial density of states (PDOS) of $\text{Na}_6\text{Sn}_3\text{P}_4\text{S}_{16}$ were studied using density functional theory (DFT) calculations to investigate the structure–property relationship further.⁵⁵ The exchange–correlation potential of $\text{Na}_6\text{Sn}_3\text{P}_4\text{S}_{16}$ was calculated using the Perdew–Burke–Ernzerhof (PBE) functional within the generalized gradient approximation (GGA) method.⁵⁶ The following orbital electrons were treated as valence electrons: Na: $2p^6 3s^1$; Sn: $5s^2 5p^2$; P: $3s^2 3p^3$; S: $3s^2 3p^4$. The plane-wave basis set energy cutoff was 720 eV within the normal-conserving pseudo-potential (NCP) to achieve energy convergence.⁵⁷ As important parameters for IR NLO material, the theoretical SHG coefficients and birefringence (Δn) of $\text{Na}_6\text{Sn}_3\text{P}_4\text{S}_{16}$ were also calculated using a suitable scissor operator. The dipole moment and SHG-density calculations were also performed to further analyze the SHG contributions of different functional units.

Results and discussion

$\text{Na}_6\text{Sn}_3\text{P}_4\text{S}_{16}$ crystallizes in the non-centrosymmetric (NCS) trigonal space group $R3m$ (no. 160) with lattice parameters $a = b = 19.304(4)$ Å, $c = 6.181(2)$ Å and $Z = 3$. Its asymmetric unit consists of one crystallographically independent Na atom, one Sn atom, two P atoms and five S atoms, with Na1 and S2 in the Wyckoff 18c position, P1 and S1 at 3a and the other atoms (Sn1, P2, S3, S4 and S5) at 9b. Table S2 in the ESI† provides more detailed information on crystal data and structural refinement. As shown in Fig. 2b, Na atoms are coordinated with six S atoms, forming slightly distorted NaS_6 octahedra with bond lengths of 2.809(6)–3.138(7) Å. NaS_6 are linked together through shared corners and edges to create closed 6-membered rings (MRs), which allows the unique isolated pinwheel-shaped $[\text{Sn}_3(\text{PS}_4)_4]$ cluster to fill the channels and finally form the final three-dimensional (3D) structure of $\text{Na}_6\text{Sn}_3\text{P}_4\text{S}_{16}$ (Fig. 2a). In the process of experimental synthesis, we also attempted to synthesize other alkali-metal-based analogues. For example, we attempted to synthesize the hypothetical $\text{K}_6\text{Sn}_3\text{P}_4\text{S}_{16}$, but only the reported KSnPS_4 was obtained. As for (Rb,Cs)-based analogues, neither of them was synthesized in this work after we made several attempts. Seen from the structure of $\text{Na}_6\text{Sn}_3\text{P}_4\text{S}_{16}$, NaS_6 units link together to compose 6-MR tunnel structures, and isolated $[\text{Sn}_3(\text{PS}_4)_4]$ clusters are located within the tunnels. While Na cations are substituted by other alkali metals ($A = \text{K}, \text{Rb}, \text{Cs}$) with larger radii, even if their longer $A\text{--S}$ ($A = \text{K}, \text{Rb}, \text{Cs}$) bond lengths can still form 6-MRs with larger channels, these tunnel structures may not be suitable for the existence of previous $[\text{Sn}_3(\text{PS}_4)_4]$ clusters. Therefore, the introduction of other alkali metals into the structure of $\text{Na}_6\text{Sn}_3\text{P}_4\text{S}_{16}$ may destabilize the original struc-

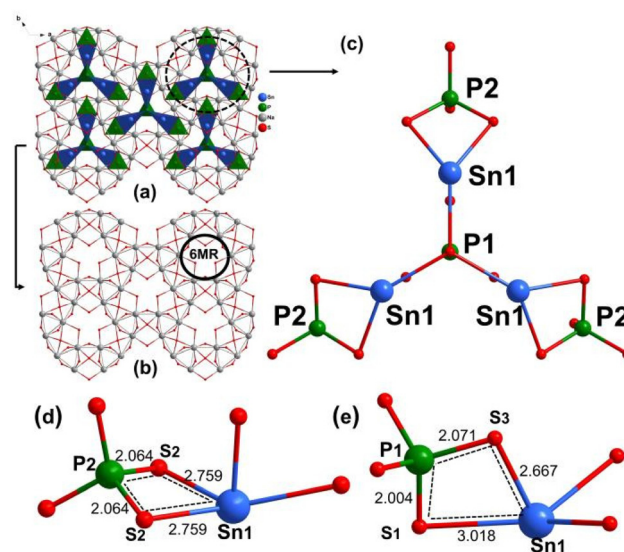


Fig. 2 (a) Whole structure of $\text{Na}_6\text{Sn}_3\text{P}_4\text{S}_{16}$ along the c -axis. (b) NaS_6 octahedra connected together to form channel-shaped closed rings. A 6-MR is indicated with black lines. (c) The pinwheel-like $[\text{Sn}_3(\text{PS}_4)_4]$ cluster consists of one $\text{P}(1)\text{S}_4$, three $\text{P}(2)\text{S}_4$, and three SnS_4 units. (d) The 4-membered ring formed by $\text{P}(2)\text{S}_4$ and SnS_4 . (e) The 4-membered ring formed by $\text{P}(1)\text{S}_4$ and SnS_4 .

tures and make it more difficult for us to achieve the experimental synthesis. Note that these $[\text{Sn}_3(\text{PS}_4)_4]$ clusters are stacked in the same direction along the c -axis, which may enhance the polarization rate and NLO effect. Sn and P atoms are quadruply coordinated with S atoms to form SnS_4 and PS_4 tetrahedra. The three SnS_4 are connected through the longest Sn–S bond to share corners, forming an $[\text{Sn}_3\text{S}_{10}]$ trimer. The coordination environment of Sn atoms can be specifically described as an irregular trigonal pyramid, which demonstrates the high distortion of SnS_4 (Fig. 2c and d). Herein, we also investigated the structures of 12 known Sn(II)-based chalcogenides in the Inorganic Crystal Structure Database (ICSD) (Table S3†) and the results show that they exhibit the following functional groups: SnS_3 ,^{58,59} SnS_4 ,^{28,60} SnS_5 ,^{61,62} SnS_6 ,⁶³ and SnS_8 .⁵² units in their structures; only $\text{Sn}_2\text{Ga}_2\text{S}_5$ ⁵⁵ and SnGa_4S_7 ²⁸ have a similar SnS_4 unit to that of titular $\text{Na}_6\text{Sn}_3\text{P}_4\text{S}_{16}$. The Sn–S bond lengths were in the range from 2.759(3) to 3.018 Å, which is also in accordance with those of 2.636(4) to 3.157(6) Å in $\text{Sn}_2\text{Ga}_2\text{S}_5$,⁶⁰ 2.6394(17) to 3.3552(21) Å in Sn_2SiS_4 ⁶³ and 2.7041(12) to 3.0180(2) Å in $\text{LaSnGa}_3\text{S}_7$.⁶² In addition, P1–S bonds are 2.071(5) Å and 2.004(12) Å, and P2–S bonds are 2.064 (4) Å, 2.032(7) Å and 2.028(6) Å, which can be also found in other thiophosphates, such as $\text{Ag}_7\text{Sn}(\text{PS}_4)_3$:⁵⁹ 2.018–2.083 Å; AgZnPS_4 :⁴³ 2.037(2) Å to 2.058(3) Å; or $\text{AgCd}_3(\text{PS}_4)_2$:⁵⁰ 2.038(3) Å to 2.064(3) Å (Fig. 2d and e). Herein, we also compared the structural differences between $\text{Na}_6\text{Sn}_3\text{P}_4\text{S}_{16}$ and SnPS_3 (Fig. 3). In SnPS_3 , Sn(II) atoms are in eight-coordinated mode with S atoms to form an $\text{Sn}(\text{II})\text{S}_8$ dodecahedron, which is different from the $\text{Sn}(\text{II})\text{S}_4$ unit in $\text{Na}_6\text{Sn}_3\text{P}_4\text{S}_{16}$. Besides, SnPS_3 exhibits a P_2S_6 unit with a P–P

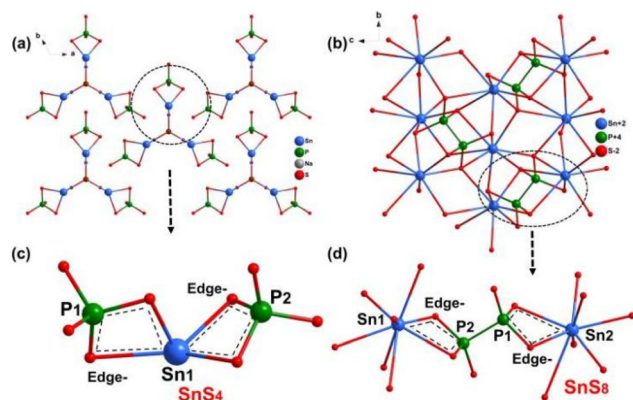


Fig. 3 (a) The combinatorial arrangement of structural units SnS_4 and PS_4 in $\text{Na}_6\text{Sn}_3\text{P}_4\text{S}_{16}$. (b) The combinatorial arrangement of structural units SnS_8 and P_2S_6 in SnPS_3 . (c) The SnS_4 and $\text{P}(1)\text{S}_4$, $\text{P}(2)\text{S}_4$ units are connected through edge sharing in the structure of $\text{Na}_6\text{Sn}_3\text{P}_4\text{S}_{16}$. (d) The $\text{Sn}(1)\text{S}_8$ and $\text{Sn}(2)\text{S}_8$ are connected to P_2S_6 units by edge sharing in the structure of SnPS_3 .

bond and P_2S_6 units connected with $\text{Sn}(\text{II})\text{S}_8$ to form a 3D network, which is also different from the 0D $[\text{Sn}_3(\text{PS}_4)_4]$ clusters in $\text{Na}_6\text{Sn}_3\text{P}_4\text{S}_{16}$.

The measured diffuse-reflectance spectrum (Fig. 4b) shows that the experimental optical bandgap of $\text{Na}_6\text{Sn}_3\text{P}_4\text{S}_{16}$ is 2.52 eV, which is consistent with its crystal color (yellow). Also, in combination with the IR transmission spectrum analysis, $\text{Na}_6\text{Sn}_3\text{P}_4\text{S}_{16}$ has a broad IR transparent region (2.5–15.0 μm) covering the two most critical atmospheric windows of 3–5 and 8–14 μm . Moreover, the presence of IR absorption peaks at 526 and 568 cm^{-1} can be attributed to P–S bond vibrations (Fig. 4c), and similar cases can be found in previously reported thiophosphates, such as AgGa_2PS_6 ⁴⁶ with IR absorption peaks at 531, 560, 580, and 590 cm^{-1} and CuCd_3PS_6 ⁶⁴ at 524, 542, and 573 cm^{-1} . The experimental Raman spectrum measured

under 532 nm laser radiation indicates that the Raman peaks (410–584 cm^{-1}) can also be attributed to the same characteristic absorption of the P–S bonding mode (Fig. 4d) as for $\text{Hg}_3\text{P}_2\text{S}_8$ ³⁴ (360–600 cm^{-1}) and $\text{K}_3\text{ReP}_2\text{S}_8$ ⁴⁵ (400–600 cm^{-1}). While the peaks at 222, 217, and 313 cm^{-1} originate from the vibration of the $\text{Sn}(\text{II})$ –S bond. In addition, the thermal behavior of $\text{Na}_6\text{Sn}_3\text{P}_4\text{S}_{16}$ was measured using a tiny custom-made vacuum-sealed silica tube, which has good thermal stability below 400 °C. As shown from its DSC curve (Fig. S2†), $\text{Na}_6\text{Sn}_3\text{P}_4\text{S}_{16}$ has an endothermic peak at 412 °C, which can be attributed as its melting point. This is much lower than the melting point of commercial IR NLO crystals (AgGaS_2 : 996 °C; ZnGeP_2 : 1298 °C). To gain insights into the intrinsic relationship between structure and properties, we performed theoretical calculations on the electronic structure and density of states (DOS) of $\text{Na}_6\text{Sn}_3\text{P}_4\text{S}_{16}$. The theoretical band structure shows a theoretical E_g of 2.05 eV for $\text{Na}_6\text{Sn}_3\text{P}_4\text{S}_{16}$ (Fig. S3a†), which is smaller than the experimental value due to the inherent defects of GGA calculations. As can be seen from the DOS diagram (Fig. S3b†), the valence band top (VB) and conduction band bottom (CB) regions are mainly occupied by S-p, Sn-p, and P-p orbitals. Therefore, optical absorption of $\text{Na}_6\text{Sn}_3\text{P}_4\text{S}_{16}$ is determined by the combined influence of $\text{Sn}(\text{II})$ S_4 and PS_4 units.

Based on the typical Kurtz–Perry method, SHG response measurement was performed under a 2.09 μm Q-switched laser with six different particle sizes. AgGaS_2 microcrystals with similar particle sizes were selected as a reference. $\text{Na}_6\text{Sn}_3\text{P}_4\text{S}_{16}$ exhibits a strong powder SHG response of about 6.6 times that of benchmark AgGaS_2 and its SHG intensities show an enhanced trend with increasing particle size, showing its essential phase-matching (PM) behaviour (Fig. 5a). It should also be noted that the SHG effect of $\text{Na}_6\text{Sn}_3\text{P}_4\text{S}_{16}$ is greater than those of other known PM IR NLO thiophosphates, such as HgCuPS_4 ($6.5 \times \text{AgGaS}_2$),⁶⁵ AgHgPS_4 ($5 \times \text{AgGaS}_2$),³⁶ KHgPS_4 ($4.15 \times \text{AgGaS}_2$),³⁵ or $\text{Hg}_3\text{P}_2\text{S}_8$ ($3.6 \times \text{AgGaS}_2$),³⁴ achieving a further breakthrough in this system. Moreover, $\text{Na}_6\text{Sn}_3\text{P}_4\text{S}_{16}$ exhibits the largest SHG response among all known IR NLO thiophosphates with bandgaps greater than 2.50 eV. We also calculated the theoretical NLO coefficient and the maximum value is about 69.3 pm/V, which is consistent with the experimental result. Furthermore, the theoretical birefringence (Δn) of $\text{Na}_6\text{Sn}_3\text{P}_4\text{S}_{16}$ was estimated to be 0.12 at a

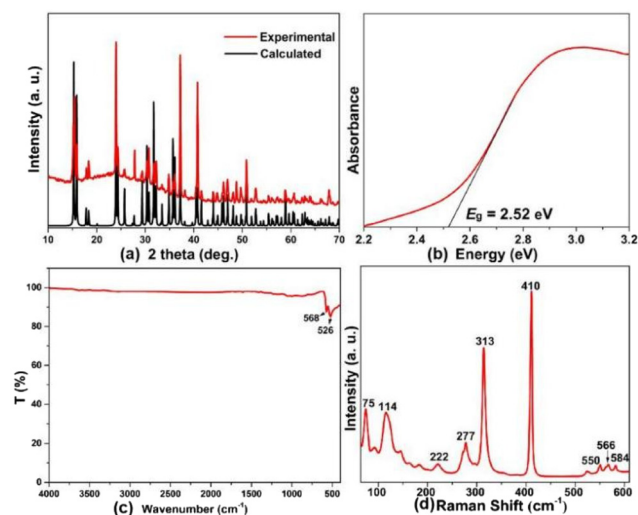


Fig. 4 Experimental XRD patterns (a), optical bandgap (b), IR spectrum (c) and Raman spectrum (d) of $\text{Na}_6\text{Sn}_3\text{P}_4\text{S}_{16}$.

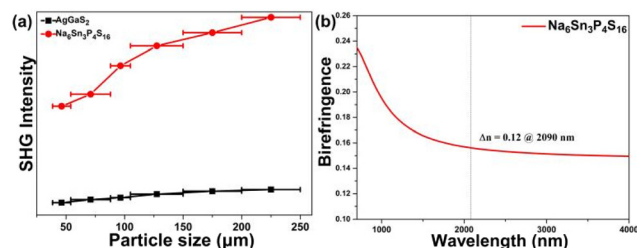


Fig. 5 (a) Powder SHG response versus particle size in $\text{Na}_6\text{Sn}_3\text{P}_4\text{S}_{16}$ with AgGaS_2 as a reference. (b) Calculated birefringence in $\text{Na}_6\text{Sn}_3\text{P}_4\text{S}_{16}$.

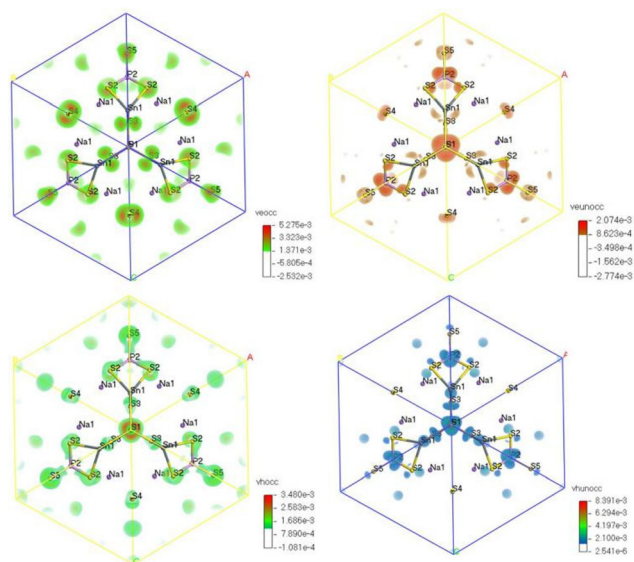


Fig. 6 Calculated SHG-density diagrams in occupied and unoccupied states of $\text{Na}_6\text{Sn}_3\text{P}_4\text{S}_{16}$.

wavelength of 2 μm (Fig. 5b), which is in good agreement with the experimental PM behavior. SHG-density calculation is also used to analyze the origin of the SHG response and the result shows that its SHG origin can be attributed to the synergistic contribution between $\text{Sn(II)}\text{S}_4$ and PS_4 units (Fig. 6). Dipole-moment calculation (Table S4†) also shows that the dipole-moment of $\text{Sn(II)}\text{S}_4$ is about twice that of the PS_4 unit, showing the huge influence of the SCALP $\text{Sn(II)}\text{S}_4$ group on the origin of the NLO response. Moreover, an electron localization function (ELF) map of $\text{Na}_6\text{Sn}_3\text{P}_4\text{S}_{16}$ was calculated and the result further confirms the existence of lone-pair orbitals for the Sn (II) atoms. Note that the stereochemically active lone-pair of an Sn(II) atom induces strong distortion in the $\text{Sn(II)}\text{S}_4$ unit and further regulates the structural anisotropy, which leads to the final large birefringence of $\text{Na}_6\text{Sn}_3\text{P}_4\text{S}_{16}$ (Fig. S4†). This work inspires us that coupling of $\text{Sn(II)}\text{S}_4$ and PS_4 units into a structure provides a feasible way to explore IR NLO candidates with strong SHG effects.

Conclusions

In summary, a promising IR NLO crystal, $\text{Na}_6\text{Sn}_3\text{P}_4\text{S}_{16}$, was successfully designed and synthesized by introducing a SCALP Sn (II) cation into the structure of a thiophosphate. $\text{Na}_6\text{Sn}_3\text{P}_4\text{S}_{16}$ exhibits the largest powder SHG response of about 6.6 times that of AgGaS_2 with PM behavior among all known PM IR NLO thiophosphates (>2.50 eV) and still maintains a relatively broad optical bandgap (2.52 eV). Theoretical calculation indicates that the synergistic contribution of edge-sharing SnS_4 and PS_4 units affords the origin of SHG, which also verifies that incorporation of an $\text{Sn(II)}\text{S}_4$ unit into thiophosphate could be regarded as an effective method to design and synthesize IR NLO crystals with large SHG effects.

Author contributions

The manuscript was written through contributions of all authors. All authors have given approval to the final version of the manuscript.

Conflicts of interest

There are no conflicts to declare.

Acknowledgements

This work was supported by the National Natural Science Foundation of China (Grant Nos. 52372009, 51872324), the Natural Science Foundation of Hebei Province (Grant No. E2020201005), the Science Foundation for Distinguished Young Scholars of Hebei Province (B2021201045), the Central Guidance on Local Science and Technology Development Fund of Hebei Province (226Z2402G).

References

- H. Lin, B.-X. Li, H. Chen, P. F. Liu, L. M. Wu, X. T. Wu and Q. L. Zhu, $\text{Sr}_5\text{ZnGa}_6\text{S}_{15}$: a new quaternary non-centrosymmetric semiconductor with a 3D framework structure displaying excellent nonlinear optical performance, *Inorg. Chem. Front.*, 2018, 5, 1458–1462.
- Y. Song, S. Cui, Z. Qian, H. Yu, Z. Hu, J. Wang, Y. Wu and H. Wu, $[\text{ASr}_4\text{Cl}][\text{Ge}_3\text{S}_{10}]$ (A = Na, K) and $[\text{KBa}_4\text{Cl}][\text{Ge}_3\text{S}_{10}]$: new salt-inclusion infrared nonlinear optical crystals with zero-dimensional $[\text{Ge}_3\text{S}_9]$ clusters, *Inorg. Chem. Front.*, 2022, 9, 5932–5940.
- H.-D. Yang, M.-Y. Ran, W.-B. Wei, X.-T. Wu, H. Lin and Q.-L. Zhu, Recent advances in IR nonlinear optical chalcogenides with well-balanced comprehensive performance, *Mater. Today Phys.*, 2023, 35, 101127.
- H. Chen, M.-Y. Ran, W.-B. Wei, X.-T. Wu, H. Lin and Q.-L. Zhu, A comprehensive review on metal chalcogenides with three-dimensional frameworks for infrared nonlinear optical applications, *Coord. Chem. Rev.*, 2022, 470, 214706.
- Z. Wang, B.-W. Liu and G.-C. Guo, First polar quaternary sulphide $\text{CsLiGa}_6\text{S}_{10}$ with mixed ordered alkali cations displaying excellent infrared nonlinear optical properties, *Inorg. Chem. Front.*, 2022, 9, 6554–6560.
- J. Chen, H. Chen, F. Xu, L. Cao, X. Jiang, S. Yang, Y. Sun, X. Zhao, C. Lin and N. Ye, $\text{Mg}_2\text{In}_3\text{Si}_2\text{P}_7$: A Quaternary Diamond-like Phosphide Infrared Nonlinear Optical Material Derived from ZnGeP_2 , *J. Am. Chem. Soc.*, 2021, 143, 10309–10316.
- Z. Qian, H. Liu, Y. Zhang, H. Wu, Z. Hu, J. Wang, Y. Wu and H. Yu, The exploration of new infrared nonlinear optical crystals based on the polymorphism of BaGa_4S_7 , *Inorg. Chem. Front.*, 2022, 9, 4632–4641.

- 8 S. Bai, D. Wang, H. Liu and Y. Wang, Recent advances of oxyfluorides for nonlinear optical applications, *Inorg. Chem. Front.*, 2021, **8**, 1637–1654.
- 9 M. Mutailipu, M. Zhang, Z. Yang and S. Pan, Targeting the Next Generation of Deep-Ultraviolet Nonlinear Optical Materials: Expanding from Borates to Borate Fluorides to Fluorooxoborates, *Acc. Chem. Res.*, 2019, **52**, 791–801.
- 10 L. Dong, S. Zhang, P. Gong, F. Liang and Z. Lin, AgIn₅Se₈: a defect diamond-like non-linear optical selenide, *Inorg. Chem. Front.*, 2023, **10**, 3248–3254.
- 11 C. Li, X. Meng, Z. Li and J. Yao, Hg-based chalcogenides: An intriguing class of infrared nonlinear optical materials, *Coord. Chem. Rev.*, 2022, **453**, 214328.
- 12 N. Zhen, L. Nian, G. Li, K. Wu and S. Pan, A High Laser Damage Threshold and a Good Second-Harmonic Generation Response in a New Infrared NLO Material: LiSm₃SiS₇, *Crystals*, 2016, **6**, 121.
- 13 M. Xia, C. Tang and R. Li, Rb₄Li₂TiOGe₄O₁₂: A Titanyl Nonlinear Optical Material with the Widest Transparency Range, *Angew. Chem.*, 2019, **131**, 18425–18428.
- 14 B. Tell and H. M. Kasper, Optical and Electrical Properties of AgGaS₂ and AgGaSe₂, *Phys. Rev. B: Solid State*, 1971, **4**, 4455–4459.
- 15 G. D. Boyd, E. Buehler and F. G. Storj, Linear and non-linear optical properties of ZnGeP₂ and CdSe, *Appl. Phys. Lett.*, 2003, **18**, 301–304.
- 16 W. Zhou, M. Geng, M. Yan, N.-T. Suen, W. Liu and S.-P. Guo, Alkali metal partial substitution-induced improved second-harmonic generation and enhanced laser-induced damage threshold for Ag-based sulfides, *Inorg. Chem. Front.*, 2022, **9**, 3779–3787.
- 17 Y.-J. Lin, R. Ye, L.-Q. Yang, X.-M. Jiang, B.-W. Liu, H.-Y. Zeng and G.-C. Guo, BaMnSnS₄ and BaCdGeS₄: infrared nonlinear optical sulfides containing highly distorted motifs with centers of moderate electronegativity, *Inorg. Chem. Front.*, 2019, **6**, 2365–2368.
- 18 J.-X. Zhao, X.-M. Jiang, W.-F. Chen, S.-M. Pei, B.-W. Liu and G.-C. Guo, Li-Free ternary sulphide Cs₅Ga₉S₁₆ with excellent nonlinear optical performance similar to classic LiGaS₂, *Inorg. Chem. Front.*, 2022, **9**, 4624–4631.
- 19 K. Wu and S. Pan, A review on structure-performance relationship toward the optimal design of infrared nonlinear optical materials with balanced performances, *Coord. Chem. Rev.*, 2018, **377**, 191–208.
- 20 S.-P. Guo, Y. Chi and G.-C. Guo, Recent achievements on middle and far-infrared second-order nonlinear optical materials, *Coord. Chem. Rev.*, 2017, **335**, 44–57.
- 21 H. Lin, W.-B. Wei, H. Chen, X.-T. Wu and Q.-L. Zhu, Rational design of infrared nonlinear optical chalcogenides by chemical substitution, *Coord. Chem. Rev.*, 2020, **406**, 213150.
- 22 J. Xu, K. Wu, B. Zhang, H. Yu and H. Zhang, LaAeAl₃S₇ (Ae = Ca, Sr): Cairo pentagonal layered thioaluminates achieving a good balance between a strong second harmonic generation response and a wide bandgap, *Inorg. Chem. Front.*, 2023, **10**, 2045–2052.
- 23 W. Wang, D. Mei, F. Liang, J. Zhao, Y. Wu and Z. Lin, Inherent laws between tetrahedral arrangement pattern and optical performance in tetrahedron-based mid-infrared nonlinear optical materials, *Coord. Chem. Rev.*, 2020, **421**, 213444.
- 24 K. Wu, Z. Yang and S. Pan, Na₂BaMQ₄ (M=Ge, Sn; Q=S, Se): Infrared Nonlinear Optical Materials with Excellent Performances and that Undergo Structural Transformations, *Angew. Chem., Int. Ed.*, 2016, **55**, 6713–6715.
- 25 A. K. Iyer, J. B. Cho, M. J. Waters, J. S. Cho, B. M. Oxley, J. M. Rondinelli, J. I. Jang and M. G. Kanatzidis, Ba₂MAsQ₅ (Q = S and Se) Family of Polar Structures with Large Second Harmonic Generation and Phase Matchability, *Chem. Mater.*, 2022, **34**, 5283–5293.
- 26 H. Lin, Y.-Y. Li, M.-Y. Li, Z. Ma, L.-M. Wu, X.-T. Wu and Q.-L. Zhu, Centric-to-acentric structure transformation induced by a stereochemically active lone pair: a new insight for design of IR nonlinear optical materials, *J. Mater. Chem. C*, 2019, **7**, 4638–4643.
- 27 Y. Xiao, M.-M. Chen, Y.-Y. Shen, P.-F. Liu, H. Lin and Y. Liu, A₃Mn₂Sb₃S₈ (A = K and Rb): a new type of multifunctional infrared nonlinear optical material based on unique three-dimensional open frameworks, *Inorg. Chem. Front.*, 2021, **8**, 2835–2843.
- 28 Z.-Z. Luo, C.-S. Lin, H.-H. Cui, W.-L. Zhang, H. Zhang, Z.-Z. He and W.-D. Cheng, SHG Materials SnGa₄Q₇ (Q = S, Se) Appearing with Large Conversion Efficiencies, High Damage Thresholds, and Wide Transparencies in the Mid-Infrared Region, *Chem. Mater.*, 2014, **26**, 2743–2749.
- 29 R. Yin, C. Hu, B.-H. Lei, S. Pan and Z. Yang, Lone pair effects on ternary infrared nonlinear optical materials, *Phys. Chem. Chem. Phys.*, 2019, **21**, 5142–5147.
- 30 X. Dong, Q. Jing, Y. Shi, Z. Yang, S. Pan, K. R. Poeppelmeier, J. Young and J. M. Rondinelli, Pb₂Ba₃(BO₃)₃Cl: A Material with Large SHG Enhancement Activated by Pb-Chelated BO₃ Groups, *J. Am. Chem. Soc.*, 2015, **137**, 9417–9422.
- 31 K. Wu, Z. Yang and S. Pan, Na₂Hg₃M₂S₈ (M = Si, Ge, and Sn): New Infrared Nonlinear Optical Materials with Strong Second Harmonic Generation Effects and High Laser-Damage Thresholds, *Chem. Mater.*, 2016, **28**, 2795–2801.
- 32 H.-D. Yang, S.-H. Zhou, M.-Y. Ran, X.-T. Wu, H. Lin and Q.-L. Zhu, Melilite oxychalcogenide Sr₂FeGe₂OS₆: a phase-matching IR nonlinear optical material realized by isomorphous substitution, *Inorg. Chem. Front.*, 2023, **10**, 2030–2038.
- 33 Y. Zhang, H. Wu, Z. Hu, J. Wang, Y. Wu and H. Yu, Achieving a strong second harmonic generation response and a wide band gap in a Hg-based material, *Inorg. Chem. Front.*, 2022, **9**, 4075–4080.
- 34 Y. Chu, P. Wang, H. Zeng, S. Cheng, X. Su, Z. Yang, J. Li and S. Pan, Hg₃P₂S₈: A New Promising Infrared Nonlinear Optical Material with a Large Second-Harmonic Generation and a High Laser-Induced Damage Threshold, *Chem. Mater.*, 2021, **33**, 6514–6521.

- 35 W. Xing, C. Tang, P. Gong, J. Wu, Z. Lin, J. Yao, W. Yin and B. Kang, Investigation into Structural Variation from 3D to 1D and Strong Second Harmonic Generation of the AHgPS_4 ($A^+ = \text{Na}^+, \text{K}^+, \text{Rb}^+, \text{Cs}^+$) Family, *Inorg. Chem.*, 2021, **60**, 18370–18378.
- 36 W. Xing, N. Wang, C. Tang, C. Li, Z. Lin, J. Yao, W. Yin and B. Kang, From AgGaS_2 to AgHgPS_4 : vacancy defects and highly distorted HgS_4 tetrahedra double-induced remarkable second-harmonic generation response, *J. Mater. Chem. C*, 2021, **9**, 1062–1068.
- 37 W. Zhou, B. Li, W. Liu and S.-P. Guo, $\text{A}(\text{Ag}_2\text{PS}_4)$ ($A = \text{K}, \text{Na/K}$): the first-type of noncentrosymmetric alkali metal Ag-based thiophosphates exhibiting excellent second-order nonlinear optical performances, *Inorg. Chem. Front.*, 2022, **9**, 4990–4998.
- 38 W. Xing, C. Tang, N. Wang, C. Li, E. Uykur, J. Wu, Z. Lin, J. Yao, W. Yin and B. Kang, $\text{AXHg}_3\text{P}_2\text{S}_8$ ($A = \text{Rb}, \text{Cs}; X = \text{Cl}, \text{Br}$): New Excellent Infrared Nonlinear Optical Materials with Mixed-Anion Chalcogenide Groups of Trigonal Planar $[\text{HgS}_2\text{X}]^{3-}$ and Tetrahedral $[\text{HgS}_3\text{X}]^{5-}$, *Adv. Opt. Mater.*, 2021, **9**, 2100563.
- 39 L. Gao, Y. Chu, X. Wu, B. Zhang and K. Wu, From thiophosphate to chalcogenide: mixed-anion AgS_xCl_y ligands concurrently enhancing nonlinear optical effects and laser-damage threshold, *Chem. Commun.*, 2021, **57**, 8218–8221.
- 40 Z. Li, S. Zhang, Z. Huang, L.-D. Zhao, E. Uykur, W. Xing, Z. Lin, J. Yao and Y. Wu, Molecular Construction from AgGaS_2 to CuZnPS_4 : Defect-Induced Second Harmonic Generation Enhancement and Cosubstitution-Driven Band Gap Enlargement, *Chem. Mater.*, 2020, **32**, 3288–3296.
- 41 Z. Li, X. Jiang, M. Zhou, Y. Guo, X. Luo, Y. Wu, Z. Lin and J. Yao, $\text{Zn}_3\text{P}_2\text{S}_8$: A Promising Infrared Nonlinear-Optical Material with Excellent Overall Properties, *Inorg. Chem.*, 2018, **57**, 10503–10506.
- 42 V. Nguyen, B. Ji, K. Wu, B. Zhang and J. Wang, Unprecedented mid-infrared nonlinear optical materials achieved by crystal structure engineering, a case study of KXP_2S_6 ($X = \text{Sb}, \text{Bi}, \text{Ba}$), *Chem. Sci.*, 2022, **13**, 2640–2648.
- 43 M. Zhou, L. Kang, J. Yao, Z. Lin, Y. Wu and C. Chen, Midinfrared Nonlinear Optical Thiophosphates from LiZnPS_4 to AgZnPS_4 : A Combined Experimental and Theoretical Study, *Inorg. Chem.*, 2016, **55**, 3724–3726.
- 44 B. Ji, A. Sarkar, K. Wu, A. Swindle and J. Wang, $\text{A}_2\text{P}_2\text{S}_6$ ($A = \text{Ba}$ and Pb): a good platform to study the polymorph effect and lone pair effect to form an acentric structure, *Dalton Trans.*, 2022, **51**, 4522–4531.
- 45 X. Tian, Y. Xiao, B. Zhang, D. Yang and K. Wu, Novel structural transformation in $\text{K}_3\text{ReP}_2\text{S}_8$ thiophosphates originating from the rare-earth (Re) cation sizes induced local coordination asymmetry, *Mater. Today Phys.*, 2022, **28**, 100885.
- 46 J. H. Feng, C. L. Hu, X. Xu, B. X. Li, M. J. Zhang and J. G. Mao, AgGa_2PS_6 : A New Mid-Infrared Nonlinear Optical Material with a High Laser Damage Threshold and a Large Second Harmonic Generation Response, *Chem. – Eur. J.*, 2017, **23**, 10978–10982.
- 47 X. Huang, S. H. Yang, X. H. Li, W. Liu and S. P. Guo, $\text{Eu}_2\text{P}_2\text{S}_6$: The First Rare-Earth Chalcogenophosphate Exhibiting Large Second-Harmonic Generation Response and High Laser-Induced Damage Threshold, *Angew. Chem., Int. Ed.*, 2022, **61**, e202206791.
- 48 J. Feng, C.-L. Hu, B. Li and J.-G. Mao, LiGa_2PS_6 and LiCd_3PS_6 : Molecular Designs of Two New Mid-Infrared Nonlinear Optical Materials, *Chem. Mater.*, 2018, **30**, 3901–3908.
- 49 C. Crokek, B. Ji, A. Sarkar, F. Wang, T. H. Syed, W. Wei, S.-P. Guo and J. Wang, Revisiting two thiophosphate compounds constituting d0 transition metal HfP_2S_6 and d^{10} transition metal $\alpha\text{-Ag}_4\text{P}_2\text{S}_6$ as multifunctional materials for combining second harmonic generation response and photocurrent response, *CrystEngComm*, 2023, **25**, 1175–1185.
- 50 Y. H. Fan, X. M. Jiang, B. W. Liu, S. F. Li, W. H. Guo, H. Y. Zeng, G. C. Guo and J. S. Huang, Phase Transition and Second Harmonic Generation in Thiophosphates $\text{Ag}_2\text{Cd}(\text{P}_2\text{S}_6)$ and $\text{AgCd}_3(\text{PS}_4)_2$ Containing Two Second-Order Jahn-Teller Distorted Cations, *Inorg. Chem.*, 2017, **56**, 114–124.
- 51 M.-Z. Li, L.-T. Jiang, S.-M. Pei, B.-W. Liu, X.-M. Jiang and G.-C. Guo, $\text{A}_2\text{Zn}_3\text{P}_4\text{S}_{13}$ ($A = \text{Rb}$ and Cs): First Infrared Nonlinear Optical Materials with Mixed Thiophosphate Functional Motifs PS_4 and P_2S_6 , *J. Mater. Chem. C*, 2022, **10**, 9146–9151.
- 52 Z. H. Shi, M. Yang, W. D. Yao, W. Liu and S. P. Guo, SnPQ_3 ($Q = \text{S}, \text{Se}, \text{S/Se}$): A Series of Lone-Pair Cationic Chalcogenophosphates Exhibiting Balanced NLO Activity Originating from SnQ_8 Units, *Inorg. Chem.*, 2021, **60**, 14390–14398.
- 53 G. M. Sheldrick, SHELXT - integrated space-group and crystal-structure determination, *Acta Crystallogr., Sect. A: Found. Adv.*, 2015, **71**, 3–8.
- 54 A. Spek, Single-Crystal Structure Validation with the Program PLATON, *J. Appl. Crystallogr.*, 2003, **36**, 7–13.
- 55 S. J. Clark, M. D. Segall, C. J. Pickard, P. J. Hasnip, M. I. J. Probert, K. Refson and M. C. Payne, First principles methods using CASTEP, *Z. Kristallogr.*, 2005, **220**, 567–570.
- 56 J. P. Perdew, K. Burke and M. Ernzerhof, Generalized Gradient Approximation Made Simple, *Phys. Rev. Lett.*, 1996, **77**, 3865–3868.
- 57 J. S. Lin, A. Qteish, M. C. Payne and V. Heine, Optimized and transferable nonlocal separable ab initio pseudopotentials, *Phys. Rev. B: Condens. Matter Mater. Phys.*, 1993, **47**, 4174–4180.
- 58 S. Banerjee, C. D. Malliakas and M. G. Kanatzidis, New layered tin(II) thiophosphates ASnPS_4 ($A = \text{K}, \text{Rb}, \text{Cs}$): synthesis, structure, glass formation, and the modulated CsSnPS_4 , *Inorg. Chem.*, 2012, **51**, 11562–11573.
- 59 Y. H. Fan, H. Y. Zeng, X. M. Jiang, M. J. Zhang, B. W. Liu, G. C. Guo and J. S. Huang, Thiophosphates Containing Ag^+ and Lone-Pair Cations with Interchiral Double Helix Show Both Ionic Conductivity and Phase Transition, *Inorg. Chem.*, 2017, **56**, 962–973.

- 60 M.-Y. Li, B. Li, H. Lin, Z. Ma, L.-M. Wu, X.-T. Wu and Q.-L. Zhu, $\text{Sn}_2\text{Ga}_2\text{S}_5$: A Polar Semiconductor with Exceptional Infrared Nonlinear Optical Properties Originating from the Combined Effect of Mixed Asymmetric Building Motifs, *Chem. Mater.*, 2019, **31**, 6268–6275.
- 61 Z. Lin, C. Li, L. Kang, Z. Lin, J. Yao and Y. Wu, $\text{SnGa}_2\text{GeS}_6$: synthesis, structure, linear and nonlinear optical properties, *Dalton Trans.*, 2015, **44**, 7404–7410.
- 62 J. Tang, W. Xing, K. Kang, T. Zeng, W. Yin and B. Kang, Quaternary rare-earth sulfide $\text{LaSnGa}_3\text{S}_7$: Synthesis, structure, thermal and optical properties, *J. Alloys Compd.*, 2020, **828**, 154380.
- 63 C. Li, Z. Lin, L. Kang, Z. Lin, H. Huang, J. Yao and Y. Wu, Sn_2SiS_4 , synthesis, structure, optical and electronic properties, *Opt. Mater.*, 2015, **47**, 379–385.
- 64 Z. Li, S. Zhang, W. Xing, Y. Guo, C. Li, Z. Lin, J. Yao and Y. Wu, Mixed-metal thiophosphate CuCd_3PS_6 : an infrared nonlinear optical material activated by its three-in-one tetrahedra-stacking architecture, *J. Mater. Chem. C*, 2020, **8**, 5020–5024.
- 65 M.-Y. Li, Z. Ma, B. Li, X.-T. Wu, H. Lin and Q.-L. Zhu, HgCuPS_4 : An Exceptional Infrared Nonlinear Optical Material with Defect Diamond-like Structure, *Chem. Mater.*, 2020, **32**, 4331–4339.